

Forces that control self-organization of chemically-propelled Janus tori

Jiyuan Wang^{1,2} , Mu-Jie Huang², Remmi D. Baker-Sediako³, Raymond Kapral²  [✉] & Igor S. Aranson⁴  [✉]

Control of the individual and collective behavior of self-propelled synthetic micro-objects has immediate application for nanotechnology, robotics, and precision medicine. Despite significant progress in the synthesis and characterization of self-propelled Janus (two-faced) particles, predictive understanding of their behavior remains challenging, especially if the particles have anisotropic forms. Here, by using molecular simulation, we describe the interactions of chemically-propelled microtori near a wall. The results show that a torus hovers at a certain distance from the wall due to a combination of gravity and hydrodynamic flows generated by the chemical activity. Moreover, electrostatic dipolar interactions between the torus and the wall result in a spontaneous tilt and horizontal translation, in a qualitative agreement with experiment. Simulations of the dynamics of two and four tori near a wall provide evidence for the formation of stable self-propelled bound states. Our results illustrate that self-organization at the microscale occurs due to a combination of multiple factors, including hydrodynamic, chemical, electrostatic and steric interactions.

¹School of Electrical and Control Engineering, Heilongjiang University of Science and Technology, Harbin 150022, P. R. China. ²Chemical Physics Theory Group, Department of Chemistry, University of Toronto, Toronto, ON M5S 3H6, Canada. ³Nanoscribe GmbH & Co. KG, Hermann-von-Helmholtz-Platz 6, 76344 Eggenstein-Leopoldshafen, Germany. ⁴Departments of Biomedical Engineering, Chemistry, and Mathematics, Pennsylvania State University, University Park, PA 16802, USA. [✉]email: r.kapral@utoronto.ca; isa12@psu.edu

Individual and collective behavior of self-propelled micro-objects (also called agents or motors) is the main topic of a rapidly expanding field termed active matter^{1–10}. Recent research on synthetic active particles has demonstrated that they possess diverse functionalities which are similar to those found in the living world, such as propulsion and energy conversion^{11,12}, artificial chemotaxis^{13–15}, rheotaxis^{16,17}, etc. However, most of the synthetic realizations of self-propelled particles lack the fidelity and efficiency of biological organisms. The limitations come mostly from micro-fabrication, resulting in relatively simple shapes such as spheres¹⁸ and rods¹¹, although more complex self-propelled helices have been made using glancing angle deposition¹⁹. These factors significantly restrict the range of possible applications of self-propelled micromotors in robotics, drug delivery, and precision medicine^{20–22}.

Advances in additive manufacturing and nanoscale 3D printing allow the design of particles with practically arbitrary shape, e.g., tori or propellers²³. Functionalization of the tori surfaces by platinum (Pt) and nickel (Ni) enables propulsion in hydrogen peroxide (H_2O_2) solution and a response to an applied magnetic field. Without a magnetic field, the tori (with sizes between 7 and 10 μm) sediment and hover near the bottom wall at a distance of the order 1–2 μm . Due to a spontaneous symmetry breaking of the hovering state, the tori tilt and translate parallel to the bottom with the speed of the order of few $\mu\text{m/s}$. The tori also form multiple rotating and translating bound states. If a dc magnetic field is applied parallel to the bottom wall, the tori turn perpendicular to the bottom and swim with much higher speed (10–20 $\mu\text{m/s}$) in the direction controlled by the magnetic field.

In this work we use molecular simulation to uncover fundamental mechanisms governing the organization of chemically self-propelled Janus tori near walls. There have been a number of studies of the behavior of active particles near walls^{24–29} in which various kinds of dynamical behavior have been observed. For instance, diffusiophoretically active Janus colloids near a hard wall have been shown to hover above the wall or slide along it at a constant height and a preferred tilt angle^{27,29}. Also, there have been investigations of the dynamics of more complex active agents, such as rigid swimmers constructed from linked rotating beads³⁰ and swimmers with conformational dynamics³¹, near a wall. In addition, there is body of literature that considers the dynamics of a torus in bulk solution. There are studies using analytical and numerical continuum methods of the properties of inactive tori^{32,33}, as well as investigations of active tori including a torus propelled by rotation about its centerline^{34–36}, a torus made from linked rotating beads³⁶ and a torus propelled by a diffusiophoretic mechanism³⁷.

Our investigations of the dynamics of Janus tori near a wall use multiparticle collision dynamics³⁸, a particle-based mesoscale

simulation technique for complex fluids that accurately incorporates thermal fluctuations, hydrodynamic interactions, chemical reactions, and solid inclusions^{39,40}. We show how various interaction potentials govern the behavior of several tori interacting with each other and the confining walls. We have found that all of gravitational, hydrodynamic, and chemical interactions are responsible for the hovering behavior of a torus above the bottom wall. When electrostatic dipolar interactions between the torus and the bottom wall are included, the torus tilts spontaneously and translates parallel to the bottom, in qualitative agreement with experiment. We also show how the interplay among these different interactions along with steric repulsion results in the formation of bound states of two and four tori.

Results and discussion

Active Janus torus near a wall. The simulations of the dynamics of a torus near a wall are carried out in a system with a slab geometry: the top and bottom walls of the simulation volume are parallel to the (x, y) plane and separated by a distance L_z . Periodic boundary conditions are applied in the x and y directions with $L_x = L_y$. The volume contains one or more tori with centerline radius a constructed from linked overlapping spherical beads that form a ring⁴¹. The torus beads are Janus spheres with catalytic C and noncatalytic N hemispherical faces. The solvent comprises A and B fluid particles. Catalytic reactions $A \rightarrow B$ occur on the catalytic faces of the beads. Figure 1a shows a torus oriented so that the catalytic side of the torus faces the wall. The symmetry axis of the torus is indicated by the unit vector $\hat{\mathbf{u}}$ pointing from the catalytic to noncatalytic sides of the torus. The simulation algorithm and its implementation are described in Methods.

A torus is heavier than the solvent and, due to the gravitational force \mathbf{F}_g , an inactive torus will sediment to the bottom and experience a short-range repulsive force from the wall. For an active torus where chemical reactions occur on its catalytic surface, because of the asymmetric distribution of reactants A and products B , a diffusiophoretic mechanism^{8,42–44} operates to propel the torus in solution. The magnitude and direction of the diffusiophoretic force \mathbf{F}_d on the torus depends on the interactions of the reactive species with the torus beads and the displacement from equilibrium.⁴⁴ We adopt the following convention: if the diffusiophoresis force \mathbf{F}_d is in the same direction as the $\hat{\mathbf{u}}$ -vector, i.e., towards the noncatalytic (passive) surface, it is called a backward-moving torus. If it is a direction opposite to $\hat{\mathbf{u}}$, it is a forward-moving torus. In experiment, the backward vs forward mode of propulsion is controlled by the relative thicknesses of the Pt and Ni layers²³. For example, for thin Pt layers (about 10 nm), the tori swim Pt (catalytic) side forward, whereas for the Pt layers thicker than 40 nm, the tori swim polymer (non-catalytic) side forward.

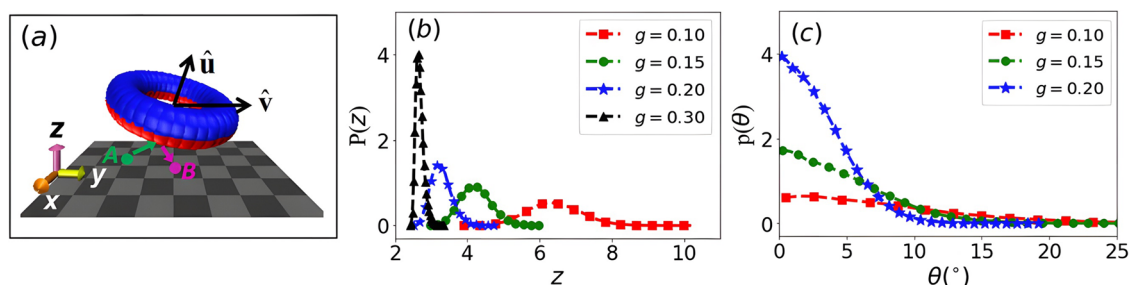


Fig. 1 Schematics of a Janus torus. **a** Janus torus with catalytic (red) and noncatalytic (blue) faces. The catalytic reaction, $A \rightarrow B$, occurs on the catalytic surface and converts fuel A particles to product B particles. The symmetry axis of the torus is indicated by the unit vector $\hat{\mathbf{u}}$ pointing from the catalytic to noncatalytic face of the torus. The vector $\hat{\mathbf{v}}$ is the center of mass (c.o.m.) velocity. **b** The probability $P(z)$ of the torus c.o.m.-wall distance for a backward-moving torus with its catalytic surface (red) facing the wall and **c** the probability distribution $p(\theta)$ vs the tilt angle θ of a backward-moving torus for various values of gravitational strength parameter g .

If a backward-moving torus is initially oriented so that its catalytic surface faces the wall as in Fig. 1a, then the gravitational and diffusiophoretic forces will have opposite signs. Consequently, the torus will be confined to the vicinity of the wall in a long-lived metastable state provided that $F_g > F_d$. If $F_g < F_d$ such an initially oriented torus can easily escape from the wall to the bulk fluid phase. If the initial orientation is opposite so that its noncatalytic surface faces the wall, then both forces act in the same direction to confine the torus to the wall in what we call a trivial metastable state. These are metastable states since sufficiently large orientational fluctuations can allow the torus to change its orientation relative to the wall, thus changing the probability of residing near the wall. A corresponding set of statements apply for forward-moving tori; for example, for $F_g > F_d$ the orientation of a forward-moving torus relative to the wall must be opposite of that of a backward-moving torus for long-lived confinement to occur. Consequently, for $F_g > F_d$ it is interesting to investigate the properties of the long-lived metastable states as a function of the strength of the confining gravitational force, and we present these results below.

The probability distribution $P(z)$ of the distance of the center of mass (c.o.m.) of the backward-moving torus from the wall is shown in Fig. 1b for several values of the gravitational strength parameter g (the value of g can be adjusted by the mass density of the torus material). For the g values in the range (0.1–0.3) presented in the figure, the torus remains confined to the vicinity of the wall and, as expected, the mean distance from the wall increases as g decreases. For $g \lesssim 0.15$, the torus beads do not experience direct repulsive interactions with the wall. This behavior indicates that the observed hovering is due to diffusiophoresis generated by chemical reactions rather than the short-range repulsive forces.

The tilt angle θ of the torus with respect to the bottom plane is determined from the scalar product of their normal vectors: $\cos(\theta) = \hat{\mathbf{u}} \cdot \hat{\mathbf{z}}$. The probability distribution of $\theta = \arccos(\hat{\mathbf{u}} \cdot \hat{\mathbf{z}})$, $p(\theta)$, normalized so that $\int_0^\pi d\theta \sin \theta p(\theta) = 1$, is shown in Fig. 1c. All distributions are peaked at the origin and broaden as g decreases, indicating larger angular fluctuations as the confinement to the wall vicinity weakens. For $g = 0.3$, the torus interacts strongly with the wall through short-range repulsive forces and $p(\theta)$ (not shown) has a very narrow peak at zero. From Fig. 1c we also see that large orientational fluctuations have very low probability because they are suppressed by interactions with the wall. Except for the largest gravitational strengths these wall interactions are diffusiophoretic in nature and do not depend strongly on direct wall repulsive forces. In the bulk fluid phase the orientational relaxation time is $\tau_r \sim 10^4$. In our simulations for times longer than τ_r we have never observed escape from these long-lived metastable states, although such escape is possible.

The forms of the concentration and fluid velocity fields that accompany the diffusiophoretic mechanism provide additional insight into the origin of torus hovering. The c_B concentration and $\mathbf{v}(\mathbf{r})$ velocity fields in the (x, z) plane near the hovering backward-moving torus with $g = 0.15$ are shown in Figs. 2a and b. The fields are displayed in a laboratory reference frame. In this frame, for the concentration, we measure the average number of product B particles in a thin slab in the (x, z) plane with thickness $\Delta = 1$ whose $y = L/2$ coordinate lies at the torus c.o.m. The z direction in this frame is the same as the $\hat{\mathbf{u}}$ vector of the torus. Similarly, the velocity field was calculated by averaging the velocities of all particles in volume elements with thickness $\Delta = 1$ in the (x, z) plane. Consequently, the fields are averages over the vertical and angular displacements that the torus experiences in its motion along the wall.

As expected, Fig. 2a shows the increased product concentration in the torus hole and near the catalytic surface. In the velocity

field plot (Fig. 2b) we observe that the solvent particles near the $C - N$ interface of the torus flow from the N to C surface. We also see that there is a suction above the torus. The solvent particles flow out along the torus bottom after they flow into the hole because the wall limits the fluid flow. There are also re-circulation regions with vortices slightly above the torus. For a hovering forward-moving torus, comparison of Fig. 2c, a shows that the magnitude of the B -particle concentration field is significantly different because the catalytic surface no longer faces the wall. Also, comparison of the corresponding fluid velocity field near a hovering forward-moving torus surface in Fig. 2d with Fig. 2b shows that the solvent particles near the $C - N$ interface flow from the C to N surfaces. In addition, there is a suction above the torus hole that pushes the fluid particles along the torus bottom surface because the wall limits the flow.

The corresponding concentration and velocity fields for backward and forward-moving tori in the bulk fluid are shown in Fig. 2e–h. Comparison of the concentration fields reveals the distortions in these fields due to the phoretically-induced interaction with the wall. The distortion of the concentration gradient affects the diffusiophoretic force and, correspondingly, the propulsion. The flow fields have a different form for hovering tori and those in the bulk fluid where for a backward-moving torus in the bulk phase the fluid flows outward from the noncatalytic surface of the torus and, after circulation, inward to the catalytic surface. While the near field velocity flow pattern for a torus bead in a cross-section of the torus is similar to that seen for a Janus colloid, the flow patterns in the vicinity of the entire torus differ from those for a spherical Janus colloid. The direction of the fluid velocity of the forward-moving torus is opposite to that for a backward-moving torus.

From these results we see that while the torus exhibits a hovering state above the wall in the presence of a gravitational field, the tilt angle distribution in Fig. 1c is centered at zero and the distribution becomes less sharply peaked as g decreases, consistent with weaker confinement that leads to enhanced thermal orientational fluctuations. Orientational fluctuations are suppressed by interactions with the wall since, if the torus tilts at fixed z , a portion of the torus will move closer to the wall and be repelled by it. Gravitational confinement prevents large changes in z as seen in Fig. 1b. The result is a dynamic hovering state where the torus is on average parallel to the wall but executes active diffusive motion due to thermally driven orientational fluctuations that produce fluctuating diffusiophoretic force components parallel to the wall.

The hovering and sliding dynamical states seen for Janus colloids near walls in the presence of a gravitational field have been shown to depend on whether the surface mobility is uniform or non-uniform^{27,29}. We have assumed uniform mobility since the solvent species have the same interactions with the catalytic and noncatalytic torus surfaces and find hovering and sliding states. Also, spherical Janus colloids will not experience the same shape-dependent effect on the orientational fluctuations as torus colloids. Nevertheless, the essential factors are wall modulations of the concentration and velocity field effects arising from self diffusiophoresis in both cases.

Effect of electrostatic forces on the torus interaction with the wall. We now show that the experimentally observed states where the torus moves along the wall with a preferred tilt angle can be modeled in the simulations by including a charge-dipolar interaction between the torus and the wall. These results are summarized in Figs. 2a–l and 3.

Experimental results reported in Baker et al.²³ suggest that a torus acquires an electric dipolar moment resulting from the electrochemical reactions occurring on the Pt surface of a torus.

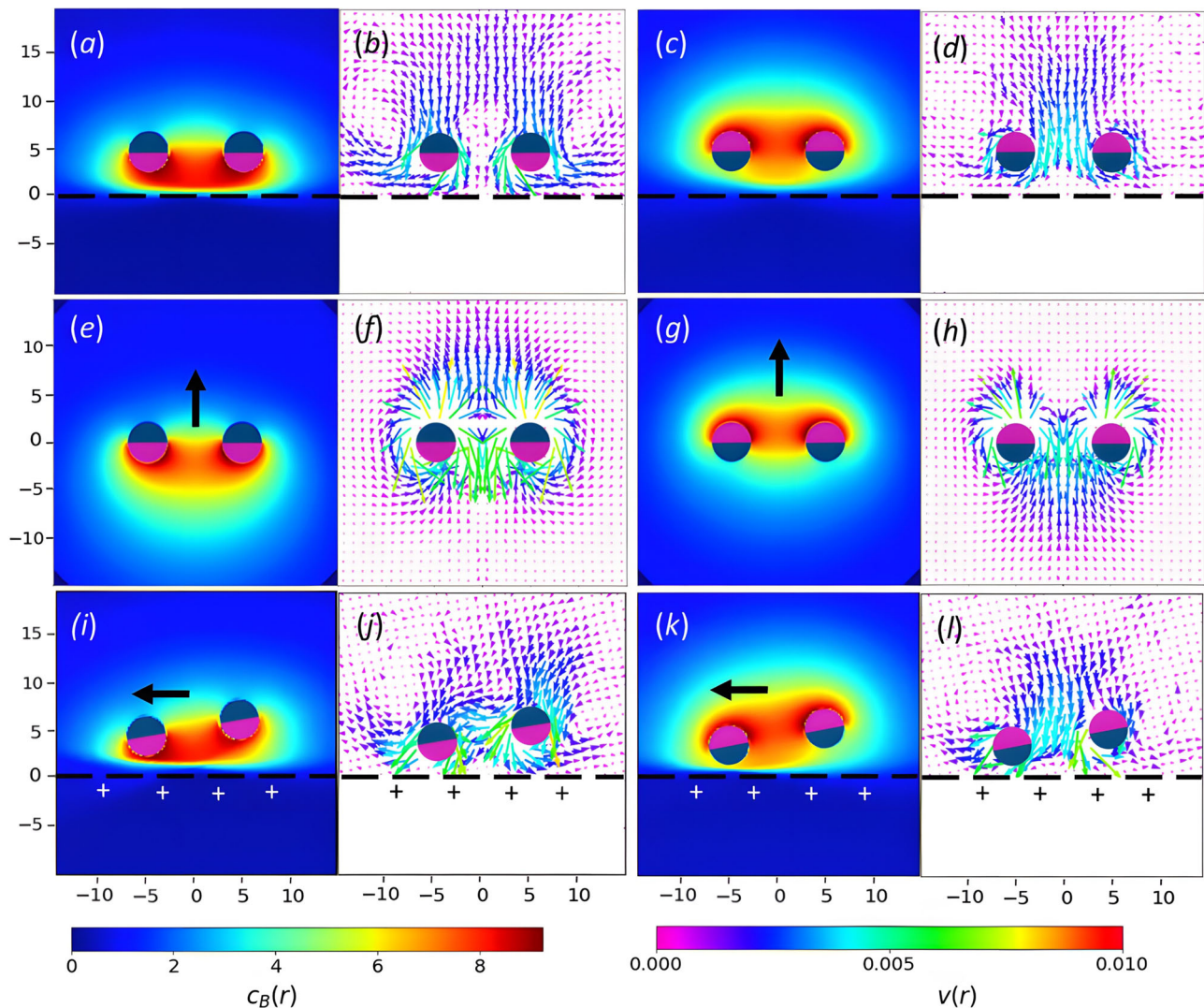


Fig. 2 Concentration and velocity fields of a torus near the wall. **a–d** The concentration $c_B(\mathbf{r})$ (**a**) and fluid velocity field $\mathbf{v}(\mathbf{r})$ (**b**) for a hovering backward-moving torus for $g = 0.15$. The concentration is shown in pseudocolor representation and the fluid velocity orientation is shown by the vectors; the colour indicates the velocity magnitude. Corresponding colour bars for the concentration and fluid velocity are displayed at the bottom of the figure. **c, d** are the same fields for a hovering forward-moving torus for $g = 0.07$. The dashed line indicates the location of the wall at $z = 0$. **e–h** (**e**) and (**f**) The concentration $c_B(\mathbf{r})$ (**e**) and fluid velocity field $\mathbf{v}(\mathbf{r})$ for a backward-moving torus in the bulk fluid (no gravitational force); **g, h** The same fields for a forward-moving torus in the bulk fluid. **i–l** Same as (**a–d**) but including the effect of charge-dipole interactions with strength $\epsilon_{cd} = 0.2$. The + symbols indicate the sign of electric charge density on the surface. For figures where a wall is present, indicated by dashed horizontal lines, the ordinates refer to the z distance from the wall, while the abscissas gives the distance x along a plane parallel to the torus orientation vector that cuts the torus through its center. The black arrows indicated the direction of motion of moving tori in all panels. The blue colour corresponds to the non-catalytic surface, and the red colour corresponds to the catalytic surface, respectively.

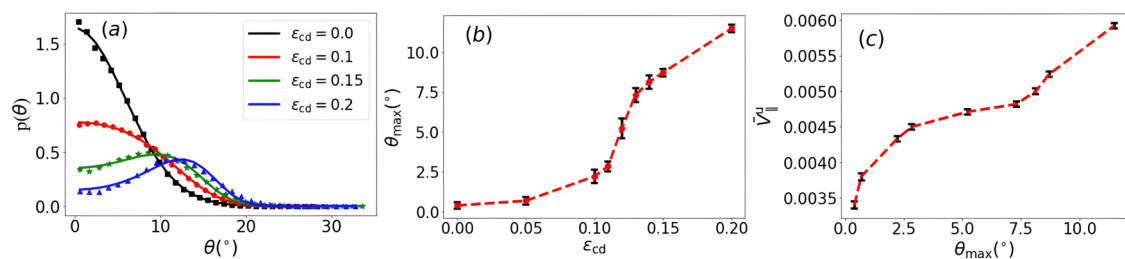


Fig. 3 The dependencies of the tilt angle and self-propelled velocity. **a** The probability distribution $p(\theta)$ versus tilt angle θ for various values of ϵ_{cd} for a backward-moving torus with $g = 0.15$. The symbols are the simulation data and the solid lines are fit according to Eq. (7) with fit parameters γ_1 and γ_2 . ($\epsilon_{cd}; \beta\gamma_1, \gamma_2$): (0.0:94, 0), (0.1:1635, 0.988), (0.15:3132, 1.015), (0.2:3686, 1.024). **b** The dependence of the tilt angle θ_{\max} versus the strength of charge-dipole interactions ϵ_{cd} . **c** The torus velocity \bar{V}_{\parallel} versus the tilt angle θ_{\max} . The probability distributions were constructed from 30–50 realizations of the dynamics. The symbols are the mean values from the 30–50 realizations, and the error bars are the standard deviations.

While direct experimental measurements of the electric dipole are not possible at this time, the supporting evidence for the dipole is two-fold: (i) A torus collected negatively charged 1 μm polystyrene spheres along its Pt surface and accumulated 2 μm positively charged latex spheres along its polymer surface, implying that the torus's platinum and polymer sides acquire opposite electric charges. (ii) Adding salt to the solution kills the effect of self-propulsion and, consequently, the ability to collect beads by the torus. This behavior is consistent with the electrohydrodynamic propulsion of the torus and the onset of the dipolar moment.

In addition, the bottom glass plate also acquires an electric charge in H_2O_2 solution. Since the torus platinum cap is conducting, due to interaction with the absorbed charges in the glass plate, the electric dipole deviates from the axial direction and orients in-plane of the torus. This interaction, in turn, results in a constant tilt angle.

Our modeling of the torus dynamics near the wall does not take into account all of the effects described above that are postulated to give rise to wall charge-torus dipolar interactions. Instead, we assume the existence of such interactions and investigate if these interactions in the presence of a gravitational force can lead to the onset of torus tilt for some specific values of the strengths of gravitational and dipolar-wall interactions. Thus, we included electric point dipoles with the strength ϵ_{cd} in the model: each bead i in the torus interacts with a uniformly charged wall through the interaction potential $V_{\text{cd}}^{(b)}(z_i)$ whose explicit form is given in the Methods section. The potential gives rise the force $\mathbf{F}_{\text{cd}} = -(\partial V_{\text{cd}}^{(b)} / \partial z_i) \hat{\mathbf{z}} \equiv \mathcal{F}_{\text{cd}} \gamma(i) \hat{\mathbf{z}}$, where $\gamma(i) = \cos(2\pi i / (N_b - 1))$ controls the sign and relative magnitude of the dipole of the N_b beads in the torus.

As one sees from Fig. 3a, for a given gravitational force, a sufficiently large electrostatic interaction results in a symmetry breaking of the horizontally hovering state and the shift of θ_{max} , the tilt angle at the maximum in $p(\theta)$, from $\theta_{\text{max}} = 0$ to $\theta_{\text{max}} > 0$. Figure 3b plots θ_{max} versus the charge-dipole strength ϵ_{cd} where it is seen that θ_{max} rises sharply from values near zero in a narrow transition region to a domain where it has large θ_{max} values that increase with further increases in ϵ_{cd} . The plot is suggestive of a bifurcation to a tilted torus beyond a critical value $\epsilon_{\text{cd}}^* \approx 0.12$ that is smoothed by thermal fluctuations. This observation is consistent with the plots in the bottom panels of Fig. 2i-l that display the concentration and velocity field plots for backward and forward moving tori with charge-dipole interactions. These fields show the asymmetries that are expected in view of tilted geometries that break the symmetry of the horizontal state.

Furthermore, a tilted torus translates parallel to the bottom wall with a velocity that depends on the tilt angle θ . To examine this effect we consider the velocity component \bar{V}_{\parallel}^u defined as follows: the projections of the motor velocity \mathbf{V} and orientation vector $\hat{\mathbf{u}}$ onto the surface plane are $\mathbf{V}_{\parallel} = \mathbf{V} \cdot \mathbf{I}_{\parallel}$ and $\mathbf{u}_{\parallel} = \hat{\mathbf{u}} \cdot \mathbf{I}_{\parallel}$, respectively, where $\mathbf{I}_{\parallel} = \mathbf{I} - \hat{\mathbf{z}}\hat{\mathbf{z}}$ and \mathbf{I} is the unit tensor. The mean velocity can be defined as $\bar{V}_{\parallel}^u = \langle \mathbf{V}_{\parallel} \cdot \mathbf{u}_{\parallel} \rangle$. Figure 3c shows that \bar{V}_{\parallel}^u increases as θ_{max} increases from zero in the presence of thermal fluctuations since any tilt from horizontal will induce motion parallel to the wall. Such orientational fluctuations are responsible for the non-zero values of \bar{V}_{\parallel}^u , even at the values of the average θ_{max} near zero seen in the figure. In the transition region \bar{V}_{\parallel}^u increases weakly since this region encompasses a small range of ϵ_{cd} , followed by a sharper increase that is proportional to θ_{max} .

Next, we develop a simple phenomenological theory for $p(\theta)$, the probability distribution of the torus tilt angle. First, we

consider the system in the absence of charge-dipole interactions where the torus hovers above the wall at some distance due to hydrodynamic and diffusiophoretic forces and is subject to a gravitational force. The orientation vector of the torus is $\hat{\mathbf{u}} = (\sin \theta \cos \phi, \sin \theta \sin \phi, \cos \theta)$. In the Cartesian frame with $\hat{\mathbf{z}}$ normal to the wall $\hat{\mathbf{z}} \cdot \hat{\mathbf{u}} = \hat{u}_z = \cos \theta$ that defines the tilt angle θ . The dynamics of the orientation vector is governed by the Langevin equation describing the dynamics of the torus,

$$\frac{d\mathbf{u}}{dt} = \zeta^{-1} \cdot (\mathbf{T}_g + \mathbf{T}_{\text{fl}}(t)) \times \mathbf{u}. \quad (1)$$

The external torque due to the diffusiophoretic forces and gravitational field is denoted by $\mathbf{T}_g = \gamma \mathbf{u} \times \hat{\mathbf{z}}$, where γ depends on the strength of the gravitational field, \mathbf{T}_{fl} is the fluctuating torque and ζ is the rotational friction tensor. The Langevin equation for the dynamics of the tilt angle can be determined from that for u_z and is given by

$$\frac{d\theta}{dt} = -\frac{\gamma}{\zeta_r} \sin \theta + \frac{1}{\zeta_r} \tilde{T}_{\text{fl}}(t), \quad (2)$$

where the fluctuating force is $\tilde{T}_{\text{fl}} = T_{\text{fl},x} \sin \phi - T_{\text{fl},y} \cos \phi$ that satisfies the fluctuation-dissipation relation $\langle \tilde{T}_{\text{fl}}(t) \tilde{T}_{\text{fl}}(t') \rangle = 2k_B T \zeta_r \delta(t - t')$. Here ζ_r is the component of the rotational friction tensor for u_z and the corresponding rotational diffusion coefficient is $D_r = k_B T / \zeta_r$. The Fokker-Planck equation reads

$$\partial_t p(\theta, t) = \partial_{\theta} \left[\frac{\gamma}{\zeta_r} \sin \theta p \right] + D_r \partial_{\theta}^2 p, \quad (3)$$

whose stationary solution is

$$p(\theta) = \mathcal{N} e^{\beta \gamma \cos \theta}, \quad (4)$$

where $\beta = 1/k_B T$ and the normalization is determined from $\int_0^{\pi} d\theta \sin \theta p(\theta) = 1$. This result may also be derived from Fokker-Planck equation that accounts for the effective orientational potential energy corresponding to u_z , $U_r(\theta) = -\gamma \cos \theta$. The expression for $p(\theta)$ in Eq. 4 is in accord with the simulation data in Fig. 1c and shows that the angle corresponding to the maximum in this distribution is $\theta_{\text{max}} = 0$.

When the electric dipolar interaction is included the torque on the torus changes and includes another contribution \mathbf{T}_{cd} , that contributes to the previous torque and contains an additional contribution that is proportional to $\cos \theta$. The Langevin equation is now given by

$$\frac{d\theta}{dt} = -\frac{\gamma_1}{\zeta_r} \sin \theta (1 - \gamma_2 \cos \theta) + \frac{1}{\zeta_r} \tilde{T}_{\text{fl}}(t), \quad (5)$$

and the corresponding Fokker-Planck equation is

$$\partial_t p(\theta, t) = \partial_{\theta} \left[\frac{\gamma_1}{\zeta_r} \sin \theta (1 - \gamma_2 \cos \theta) p \right] + D_r \partial_{\theta}^2 p, \quad (6)$$

whose stationary solution is

$$p(\theta) = \mathcal{N} e^{\beta \gamma_1 \cos \theta (1 - (\gamma_2/2) \cos \theta)}. \quad (7)$$

In this case the corresponding rotational potential energy is $U_r(\theta) = -\gamma_1 \cos \theta (1 - (\gamma_2/2) \cos \theta)$ and has a contribution proportional to $\cos^2 \theta$ that is responsible for breaking symmetry. In contrast to the situation where there are no charge-dipole interactions, now the probability distributions indicate that the angle corresponding to the maximum in the distribution is at $\theta_{\text{max}} > 0$, provided the charge-dipole strength γ_2 is sufficiently large. Figure 3a compares the angle probability distributions $p(\theta)$ for different values of the electric dipolar strength ϵ_{cd} obtained from the simulations with the predictions of Eq. 7. The simulations results are in good agreement with the analytical

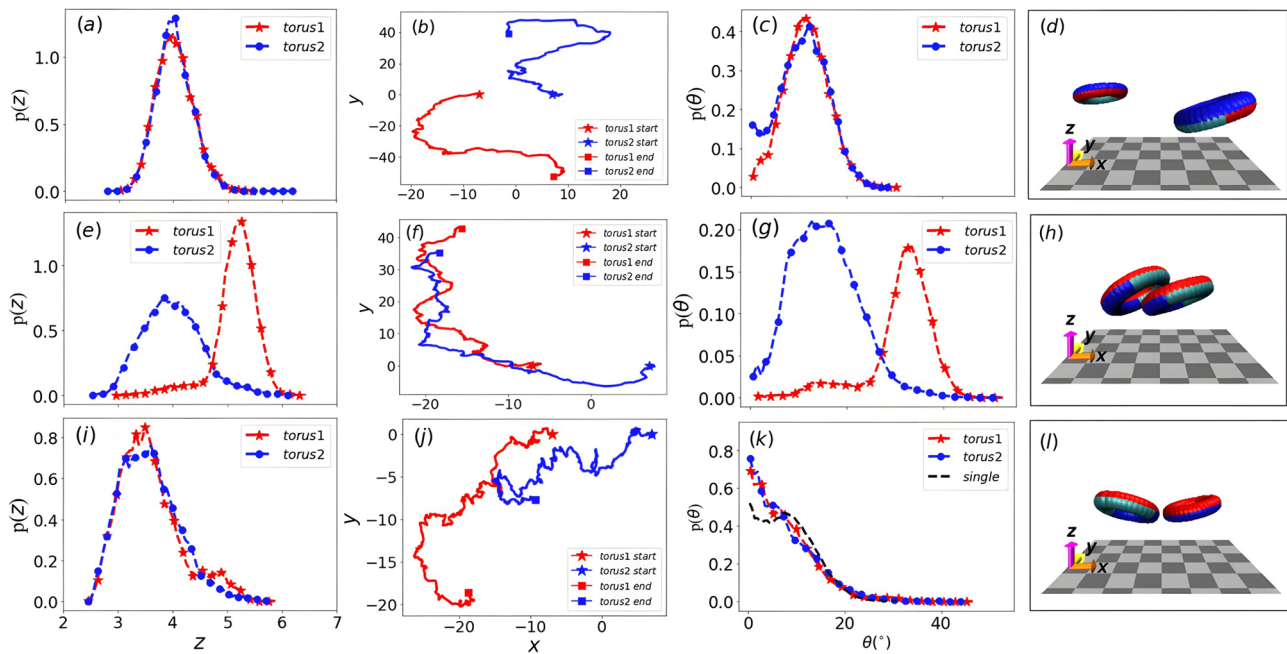


Fig. 4 Bound states of two tori near the wall. **a–d** Backward-moving tori with $g = 0.15$ and $\epsilon_{cd} = 0.2$; **e–h** forward-moving tori with $g = 0.07$ and $\epsilon_{cd} = 0.2$; **i–l** forward-moving tori with $g = 0.09$ and $\epsilon_{cd} = 0.2$. The panels **(a, e, i)** are the probability distribution $P(z)$ versus the hovering height z , **b, f, j** are the trajectories of the centers of mass of the two tori, **c, g, k** are the probability distribution $p(\theta)$ versus the tilt angle θ , **d, h, l** an instantaneous configuration of the two tori. The probability distributions were constructed from 30–40 realizations of the dynamics. The red colour indicates the catalytic surface. The blue/green facets correspond to the non-catalytic surface. The torus moves with the blue facet forward.

expression in Eq. 7 showing that this simple model captures the origin of the symmetry-breaking mechanism.

Dynamics of several tori near the wall. We now consider the dynamics of two and four interacting tori in the vicinity of the wall. The tori are subject to all the interactions discussed above for a single torus, as well as a short-range steric repulsion between beads on different tori. To accommodate several tori in configurations where they can separate sufficiently far from each other and behave independently, the size of the simulation box is increased to $60 \times 60 \times 40$. Periodic boundary conditions are again used in directions parallel to the walls.

Two tori. The simulation results for two tori near the wall are summarized in Fig. 4a–l. Using the same parameter values, $g = 0.15$ and $\epsilon_{cd} = 0.2$, as in Fig. 2 for a single hovering backward-moving torus near the wall, the results for a pair of such tori are given in Fig. 4a–d. This figure shows the probability distributions $P(z)$ vs their c.o.m. distances from the wall, z , sample trajectories of the c.o.m. positions of the two tori, and the probability distributions of the tilt angles θ for each of the two tori, $p(\theta)$. We observe that for both tori the $P(z)$ and distributions practically coincide. The $p(\theta)$ distributions also very closely correspond, and the average tilt angles are about the same as that for a single torus under the same conditions presented earlier. The trajectories show that the distances between the tori centers of mass, D , are concentrated between $D = 18$ and 28 . These results, along with the instantaneous configuration in Fig. 4d and Supplementary Video 1, support the conclusion that the tori behave independently without forming a long-lived metastable bound state. This behavior is analogous to that for backward-moving sphere-dimer⁴⁵ and Janus⁴⁶ colloids which also show little or no tendency to cluster.

By contrast, two forward-moving tori near the wall can form long-lived bound states, as we now describe. We first consider systems with $\epsilon_{cd} = 0.2$ and two values of the gravitational force:

$g = 0.07$ (again the same parameter values as in Fig. 2 for a single torus), and a larger value $g = 0.09$. The results for $g = 0.07$ in Fig. 4e–h indicate that the $P(z)$ and $p(\theta)$ distributions of the individual tori are no longer the same, as was the case for backward-moving tori. On average, one torus lies at a distance farther from the wall than the other; also the tilt angle is larger for the upper torus. The plot of the probability density, $P(D)$, in Fig. 5a, shows that the D values are concentrated between $D = 7.0$ and 10.0 . Since a torus has a centerline radius $a = 5$, this indicates that the two tori form a stacked bound state. These features are evident in the instantaneous configuration in Fig. 4e–h, see also Supplementary Video 2.

For $g = 0.09$, the character of the metastable bound pair changes and adopts a predominantly side-by-side structure parallel to the wall. (See Supplementary Video 3) This observation is quantified in Fig. 4i–l where we see that the $P(z)$ and $p(\theta)$ distributions for the two tori coincide, so both tori lie at similar distances from the wall, and their tilt angles are close. In contrast to the corresponding tilt angle distribution for a single forward-moving torus, $p(\theta)$ is peaked at the origin, and the tilt angles differ from that for a single torus near the wall. The $P(D)$ distribution in Fig. 5b is sharply peaked at $D \approx 14$, characteristic of a well-defined bound pair. The trajectories indicate that the bound state translates and rotates. An instantaneous configuration is shown in Fig. 4i–l.

Simulations have also been carried out for a lower value of $\epsilon_{cd} = 0.1$ and the same two values of g as above. The results show that for $g = 0.09$ the bound state again has a predominantly side-by-side structure, while for $g = 0.07$ the dynamics fluctuates between stacked and side-by-side bound states. A quantitative characterization of this behavior is given in Figs. 5c, d that plot the $P(z)$ and $p(\theta)$ distributions. One can see that the $P(z)$ distributions in Fig. 5c are intermediate between those in Figs. 4e and i, corresponding to stacked and side-by-side bound pairs: in particular the probability distribution of torus 1 has a smaller amplitude than that in Fig. 4e and a shoulder that extends into

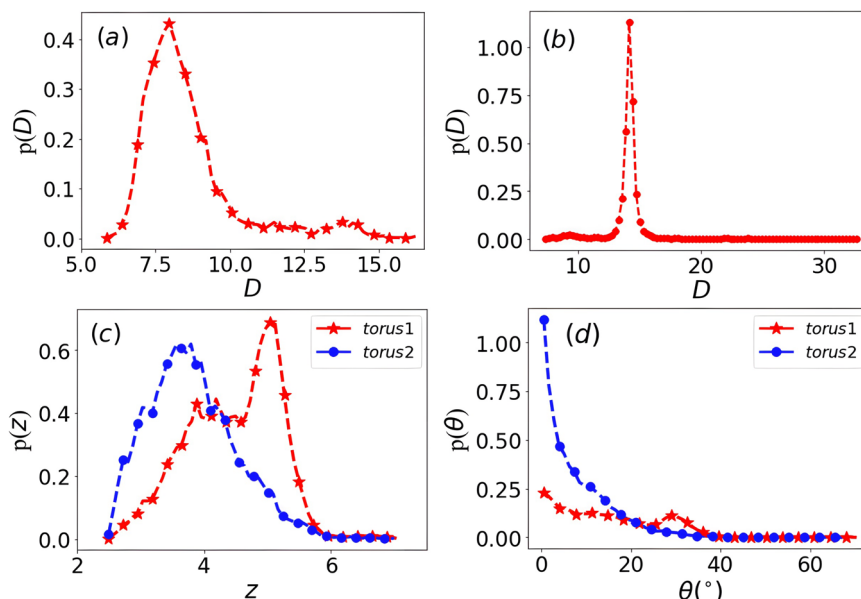


Fig. 5 Probability distributions for two tori near the wall. Probability distributions $P(D)$ for forward-moving tori with $\epsilon_{cd} = 0.2$ and $g = 0.07$ (a) and $g = 0.09$ (b). Probability distributions $P(z)$ (c) and $p(\theta)$ (d) for the parameters $\epsilon_{cd} = 0.1$; and $g = 0.07$.

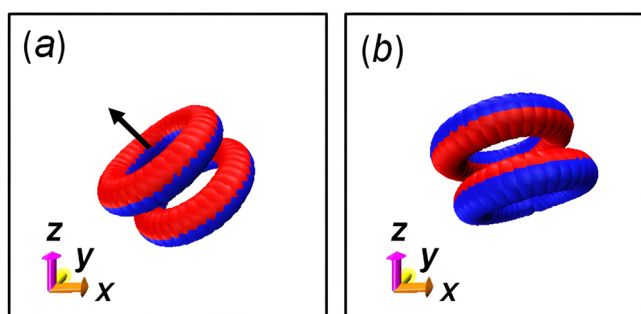


Fig. 6 Bound states of two tori in bulk solution. Instantaneous configurations showing two types of metastable bound state of two tori in bulk solution without a gravitational force: **a** propagating stacked tori with their catalytic surfaces pointing in the same direction. The black arrow indicates the direction of motion. **b** Tumbling (randomly rotating) stacked tori with their catalytic surfaces pointing towards each other. The red/blue colours correspond to catalytic/non-catalytic surfaces.

the high probability region of torus 2. The $p(\theta)$ distribution is similar to those in Fig. 4k. This behavior can be rationalized by noting that stronger gravitational confinement suppresses orientational fluctuations and causes the tori to adopt nearly side-by-side configurations parallel to the wall, while larger ϵ_{cd} values tend to induce tilt. Thus, smaller g and larger ϵ_{cd} will favor the stacked bound state.

The bound states of two forward-moving tori near the wall may be compared to the dynamics of two such tori in bulk solution in the absence of a gravitational force. Stacked bound long-lived metastable states are also observed, but they have rather different characters. Figure 6a, b show the two predominate configurations we observed. The tori that stack with their catalytic surfaces in the same direction and propagate along the common axis of the two tori are indicated by the arrow in Fig. 6a. By contrast, Fig. 6b illustrates the other configuration where the catalytic surfaces point towards each other with the noncatalytic surfaces on the outside of the bound pair. Since a forward-moving torus propagates in the

direction of its catalytic surface, this bound state does not propagate but only executes active Brownian motion with rotation. Similar bound states were observed experimentally in Baker et al.²³, Supplementary Video 6 from that paper.

Four tori. A greater variety of clustered metastable states is observed for four tori near the wall. We confine our attention to the same gravitational and charge-dipole interactions as for two tori described above, in particular, we consider $\epsilon_{cd} = 0.2$ with $g = 0.07$ and $g = 0.09$ for forward-moving tori.

Figure 7a–c shows images of two cluster configurations drawn from different realizations of the dynamics. In one of these clusters in panels (a) and (b), side and top views, respectively, one sees two side-by-side tori, where one torus is interacting with two tilted tori. A distinctive feature of this configuration is that one of these two tilted tori has flipped its orientation and its catalytic surface is now oriented towards the wall. (The dynamics of this bound state is shown in Supplementary Video 4). The other cluster shown in top view in panel (c) comprises a pair of stacked tori similar to those in Fig. 4h. Quantitative characterization of these clusters is given in Fig. 7d, e that show the $P(z)$ and $p(\theta)$ probability densities. The $P(z)$ distribution has a double-peaked structure characteristic of a stacked configuration but it more closely resembles that for $\epsilon_{cd} = 0.1$ with $g = 0.07$ in Fig. 5c. The $p(\theta)$ distribution is also similar to that in Fig. 5d, except that it extends to large angles and has a small maximum near $\theta \approx 150^{\circ}$ indicating that some tori have flipped their orientation to the wall. Thus, the statistically predominate cluster is a bound pair of two stacked tori whose structure is modified due to interactions among the four tori.

Turning next to systems of four tori with $g = 0.09$ and $\epsilon_{cd} = 0.2$, we see in Fig. 8a, b, side and top views, respectively, clusters comprising stacked and side-by-side torus pairs, and (c) two staggered interacting side-by-side pairs. (The dynamics giving rise to the bound state in Fig. 8c is shown in Supplementary Video 5.) The $P(z)$ and $p(\theta)$ probability distributions shown in Fig. 8d, e resemble those in Fig. 4i and k, indicating that clusters with two staggered interacting side-by-side pairs dominate the dynamics.

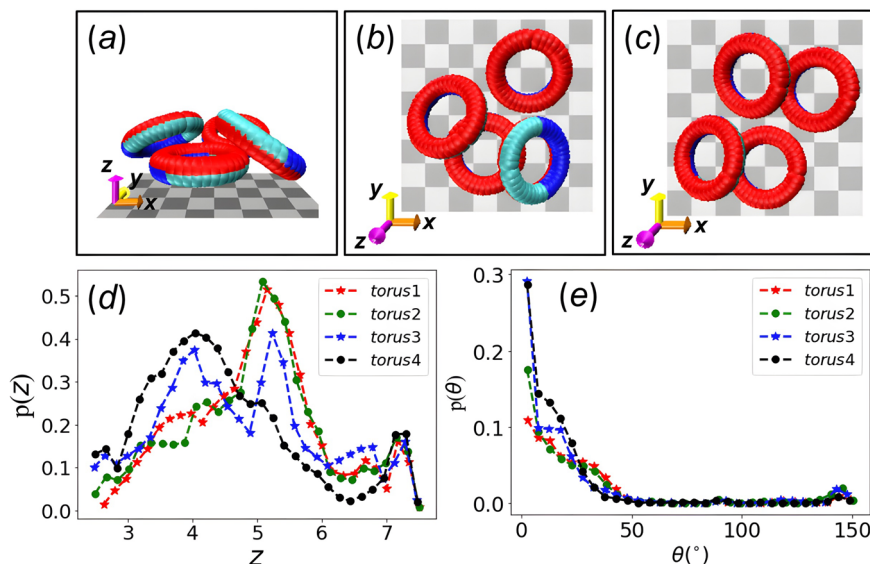


Fig. 7 Bond states of four tori near the wall for $g = 0.07, 7D2 \epsilon_{cd} = 0.2$. **a–c** Instantaneous configurations of metastable bound states of four forward-moving tori near the wall; **a** and **b** top and side views at the same time instant, **c** top view from another realization of the dynamics at a given time instant. **d–e** $P(z)$ and $p(\theta)$ probability distributions constructed from 25 realizations of the dynamics, the symbols show the mean values. The red colour indicates the catalytic surface. The blue/green facets correspond to the non-catalytic surface. The torus moves with the blue facet forward.

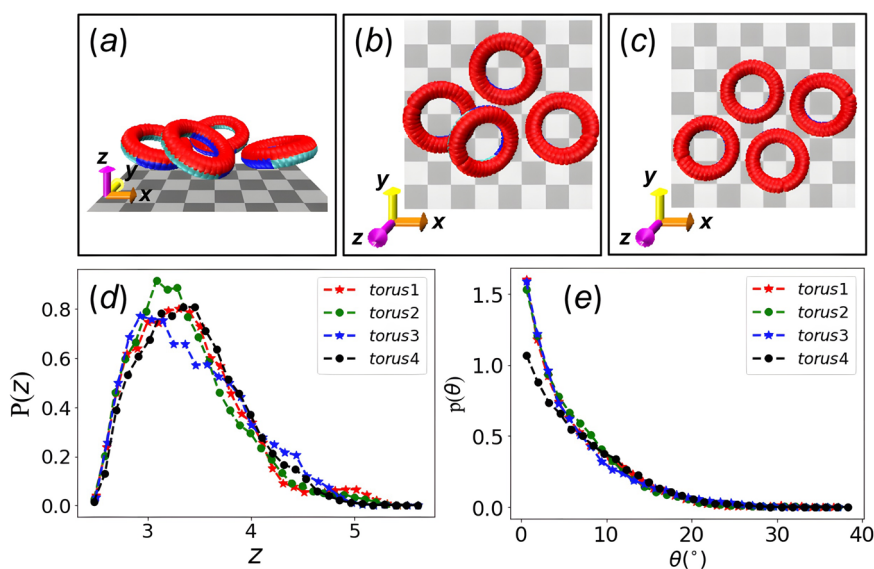


Fig. 8 Bound state for four tori near the wall for $g = 0.09, 7D2 \epsilon_{cd} = 0.2$. **a–c** Instantaneous configurations of metastable bound states of four forward-moving tori near the wall; **a** and **b** top and side views at the same time instant, **c** top view from another realization of the dynamics at a given time instant. **d–e** $P(z)$ and $p(\theta)$ probability distributions constructed from 25 realizations of the dynamics, the symbols show the mean values. The red colour indicates the catalytic surface. The blue/green facets correspond to the non-catalytic surface. The torus moves with the blue facet forward.

Thus, for these two and four tori systems, a number of different long-lived bound metastable states exist whose structure depends both on parameters that control their interactions with the wall and on steric forces that reflect the torus geometry. The geometry of the torus influences the concentration and flow fields in its vicinity and their interactions with the walls and other tori. This gives rise to multi-torus configurations that differ from those of simple spheres or dimer motors.

Conclusions

We have shown that a variety of forces control the behavior of chemically-propelled torus colloids near walls. They include gravitational, steric-repulsive, diffusiophoretic, hydrodynamic,

and electrostatic forces. If we neglect any of the forces, then the experimentally observed behavior cannot be reproduced. For example, no persistent horizontal translation near the wall can be obtained without electrostatic interaction. Our simulations also make a prediction that backward moving tori do not form bound states (see Fig. 4a–d). Another important prediction from our work is that, depending on the gravitational strength, a transition from stacked bound states (Fig. 4e–h) to flattened side-by-side bound states (Fig. 4i–l) occurs. In turn, the effective mass density can be controlled by depositing more catalyst (Pt), making the particles heavier. Alternatively, 3D printing hollow particles will make them lighter. The existence of metastable bound states of different types for four tori that depend on the magnitudes of the gravitational and charge-dipole interactions, suggests that

interesting regular and more complex collective tori states could be found in systems with large numbers of interacting tori near a wall. The algorithms developed here can be applied to particles of different shapes (e.g., propellers, helices, etc.) or more complex chemical reactions. In addition to electrostatic forces, magnetic interactions can be included as well.

Methods

Details of the MPCD algorithm. The simulations are carried out using a mesoscopic particle-based method. The dynamics of the torus motors and fluid particles are explicitly taken into account by combining molecular dynamics with multiparticle collision dynamics for the interactions among the fluid particles. Chemical reactions on the catalytic part of the torus surface and in the bulk of the fluid are also incorporated in this dynamical method. On long distance and time scales, the method has been shown to yield the Navier-Stokes and reaction-diffusion equations with analytical expressions for the transport coefficients^{38–40,47}. Consequently, all relevant properties such as local velocity and concentration fields, as well as torus dynamical properties, can be extracted directly from the simulations from averages of the particle dynamics. Additional details of the simulation methods are given below.

The simulation box has dimensions $L_x = L_y = L_z = 40$ (or $L_x = L_y = 60$ and $L_z = 40$ for systems with more than a single torus) and contains $N_s = N_A + N_B$ solvent particles with mass m . A torus is constructed from linked spherical beads as described earlier⁴¹. Briefly, a torus is made from N_b spherical beads with radius r_b linked to form a ring. Although there are soft repulsive potential interactions between the beads and solvent particles, the solvent cannot penetrate into a bead closer than r_b , which is used to define its radius. The tori with a centerline radius $a = 5$ considered in this work were made from $N_b = 39$ beads, and the segmented structure that results from the overlapping linked beads with radius r_b is visible in Fig. 1a. The neighboring beads in this ring are connected by harmonic springs with spring constant $k_s = 500$. The equilibrium bond length between the i th and $(i + j)$ th beads is $r_{ij}^{i+j} = 2a \sin(j\pi/N_b)$, $j = 1, 2, \dots, N_b/2$. The torus has mass $M_{39} = 3890$. While, the frictional and propulsion properties of a torus in bulk solution we described earlier, here we consider situations that are similar to the experimental studies where one or more tori experience gravitational and charge-dipolar interactions with a wall, which lead to new phenomena. The interactions the tori experience are given below.

The A and B fluid particles undergo bounce-back collisions with the walls, and interact with each bead in a torus motor through short-range repulsive Lennard-Jones potentials. The particles interact among themselves through multiparticle collisions³⁸. The torus motor interacts with the bottom wall through a short-range repulsive Lennard-Jones wall potential energy function. We also consider situations where the wall has a positive charge density and a torus has nonuniform distribution of point dipoles. In this case we also have charge density-dipole interactions for each bead with the wall. To account for the effect of gravity on the motor and the possible inhomogeneous distribution of mass due to the different compositions of the catalytic and noncatalytic portions of the beads, we have a gravitational potential energy function.

More specifically, these potential energy functions have the following forms: The $\alpha = \{A, B\}$ particles interact with the torus beads through the potential $V_\alpha^{(b)}(r_{ki})$ with strength ϵ_α , where $r_{ki} = r_k - r_i$ is the vector from the center of torus bead i to fluid particle k of species α . The short range potential function has the form

$$V_\alpha^{(b)}(r_{ki}) = 4\epsilon_\alpha \left[\left(\frac{\sigma}{r_{ki} - r_b} \right)^{12} - \left(\frac{\sigma}{r_{ki} - r_b} \right)^6 + \frac{1}{4} \right], \quad (8)$$

for $r_{ki} \leq r_c$ where $r_c = r_b + 2\frac{1}{2}\sigma$ and zero for $r_{ki} > r_c$. We take $\sigma = 1.0$, $r_b = 1.0$. For backward-moving tori we take $\epsilon_A = 0.1\epsilon$, $\epsilon_B = \epsilon$, while for forward-moving tori these potential strengths are interchanged and $\epsilon_A = \epsilon$, $\epsilon_B = 0.1\epsilon$. Although the reactants and products interact with the torus beads with different potentials, the potentials we consider do not take into account the more generic situation where the interactions may differ for the catalytic and noncatalytic faces. Such more general interactions have been considered in particle-based simulations collective Janus colloid dynamics⁴⁶ and for a Janus colloid interacting with a wall²⁷. Each torus bead i interacts with the bottom wall through a repulsive Lennard-Jones wall potential energy function,

$$V_w^{(b)}(z_i) = \epsilon_w \left[\frac{1}{15} \left(\frac{\sigma_w}{z_i} \right)^9 - \frac{1}{2} \left(\frac{\sigma_w}{z_i} \right)^3 \right], \quad (z \geq z_{\min}), \quad (9)$$

and zero otherwise. Here z_i is the vertical distance of motor bead i from the lower wall at $z = 0$. We take $\sigma_w = 3.0$ and $\epsilon_w = 1.0$. The potential is truncated at the minimum of the potential energy function at $z_{\min} = (2/5)^{1/6} \sigma_w = 2.575$ so that the wall force vanishes for $z \geq z_{\min}$. A similar expression applies to the upper wall. The torus beads also interact with the bottom wall through charge density-dipole potential energy functions,

$$V_{cd}^{(b)}(z_i) = \frac{\epsilon_{cd}}{2} \ln((L_z^2 + z_i^2)/z_{ci}^2) \cos(2\pi i/(N_b - 1)), \quad (10)$$

where each torus bead is labeled by $i = 0, \dots, N_b - 1$ and z_{ci} is the vertical distance of motor bead i from the center of mass of the catalytic hemisphere to the bottom wall. The gravitational potential acting on a bead is given by $V_g^{(b)}(z_{ci}) = -gz_{ci}$ where g accounts for the mass and the acceleration due to gravity.

The total interaction energy is then given by

$$V(\mathbf{r}^{N_b}, \mathbf{r}^{N_s}) = \sum_{i=1}^{N_b} \left(V_w^{(b)}(z_i) + V_{cd}^{(b)}(z_i) + V_g^{(b)}(z_i) \right) + \sum_{i=1}^{N_b} \sum_{a=A}^B \sum_{k=1}^{N_s} \theta_k^\alpha V_\alpha^{(b)}(r_{ki}), \quad (11)$$

where θ_k^α is an indicator function that is one if particle k is species α and zero otherwise.

For the simulations involving several tori, we also included short-range repulsive interactions between the beads i, j of different tori,

$$V_m^{(b)}(r_{ij}) = 4\epsilon_m \left[\left(\frac{\sigma_m}{r_{ij}} \right)^{12} - \left(\frac{\sigma_m}{r_{ij}} \right)^6 + \frac{1}{4} \right], \quad (12)$$

for $r_{ij} \leq r_c$ where $r_c = 2\frac{1}{2}\sigma_m$ and zero for $r_{ij} > r_c$, where $r_{ij} = \mathbf{r}_i - \mathbf{r}_j$ is the vector from the center of torus bead i to that of bead j . We take $\sigma_m = 2(r_b + \sigma)$, $\epsilon_m = \epsilon$ in order to prevent binding due to solvent exclusion effects.

An irreversible chemical reaction, $C + A \rightarrow C + B$, takes place on the C hemispherical surface of each motor bead that converts species A to product B. The reactive events occur with probability p when an A or B particle crosses a reaction radius $R_r = r_c$. We have taken $p = 1$ but the reaction rate may be varied by changing the value of p . The fluid phase reaction that is used to maintain the system in a nonequilibrium state has rate constant $k_b = 0.001$ and is carried out using the reactive version of multiparticle collision dynamics where reactions are carried out probabilistically in each multiparticle collision cell, and the dynamics yields the reaction-diffusion equations on long distance and time scales⁴⁸.

Simulation parameters. The molecular dynamics portion of the evolution uses the velocity-Verlet algorithm with a molecular dynamics time step, $\delta t = 0.001$, and the multiparticle collision dynamics portion uses a multiparticle collision time of $\tau = 0.5$. The collision rotation angle is $\pi/2$. Grid shifting is used to insure Galilean invariance⁴⁹. The system temperature is $k_B T = 0.2$. The solvent density is $\rho_0 \approx 10$, so that the approximate number of fluid particles is given by $N_s = \rho_0 L_x L_y L_z \approx 1.44 \times 10^6$. For $\tau = 0.5$ the fluid dynamic viscosity is $\eta = 1.43$, the kinematic viscosity is $\nu = \eta/\rho = 0.143$, and the common diffusion coefficient for the A and B species is $D = 0.117$. For a torus with velocity $V = 0.006$, the Reynolds number is $Re = Va/\nu \approx 0.2$, the Peclet number is $Pe = Va/D \approx 0.25$, the Damköhler number of $Da = \kappa_+ a/D \approx 2$ signals that the reaction on the torus surface with rate constant κ_+ per unit surface area is in the diffusion-influenced regime, and the Schmidt number is $Sc \approx 1.2$ so that momentum transport is greater than mass transport. From the scaling that enters mesoscopic dynamics⁵⁰, simulations of systems with such dimensionless numbers, where fluid particles interact with solute particles through intermolecular potentials, behave as low Reynolds number fluids with liquid-like properties. This has been confirmed by simulations with a multiparticle collision time of $\tau = 0.1$ where the Reynolds number is an order of magnitude smaller and the Schmidt number is an order of magnitude larger⁴¹.

Results are reported in dimensionless units with mass m , length σ , energy ϵ , and time $t_0 = \sqrt{m\sigma^2/\epsilon}$.

Data availability

Raw data were generated at SciNet HPC Consortium computers. Derived data supporting the findings of this study are available from the corresponding author upon reasonable request.

Code availability

The computer code supporting the findings of this study are available from the corresponding author upon reasonable request.

Received: 18 December 2021; Accepted: 23 June 2022;

Published online: 06 July 2022

References

- Lauga, E. & Powers, T. R. The hydrodynamics of swimming microorganisms. *Rep. Prog. Phys.* **72**, 096601 (2009).
- Saintillan, D. & Shelley, M. J. Emergence of coherent structures and large-scale flows in motile suspensions. *J. Roy. Soc. Interface* **9**, 571–585 (2012).

3. Aranson, I. S. Collective behavior in out-of-equilibrium colloidal suspensions. *Comptes Rendus Physique* **14**, 518–527 (2013).
4. Elgeti, J., Winkler, R. G. & Gompper, G. Physics of microswimmers—single particle motion and collective behavior: a review. *Rep. Prog. Phys.* **78**, 056601 (2015).
5. Zöttl, A. & Stark, H. Emergent behavior in active colloids. *J. Phys. Condens. Matter* **28**, 253001 (2016).
6. Illien, P., Golestanian, R. & Sen, A. ‘fuelled’ motion: phoretic motility and collective behaviour of active colloids. *Chem. Soc. Rev.* **46**, 5508–5518 (2017).
7. Ramaswamy, S. Active matter. *J. Stat. Mech.* **2017**, 054002 (2017).
8. Oshanin, G., Popescu, M. N. & Dietrich, S. Active colloids in the context of chemical kinetics. *J. Phys. A: Math. Theor.* **50**, 134001 (2017).
9. Gompper, G. et al. The 2020 motile active matter roadmap. *J. Phys.: Condensed Matter* **32**, 193001 (2020).
10. Gaspard, P. & Kapral, R. Active matter, microreversibility, and thermodynamics. *Research* **2020**, 9739231 (2020).
11. Paxton, W. F. et al. Catalytic nanomotors: autonomous movement of striped nanorods. *J. Am. Chem. Soc.* **126**, 13424–13431 (2004).
12. Wang, J. & Gao, W. Nano/microscale motors: biomedical opportunities and challenges. *ACS nano* **6**, 5745–5751 (2012).
13. Stark, H. Artificial chemotaxis of self-phoretic active colloids: collective behavior. *Accounts Chemical Res.* **51**, 2681–2688 (2018).
14. Jin, C., Krüger, C. & Maass, C. C. Chemotaxis and autochemotaxis of self-propelling droplet swimmers. *Proc. Natl Acad. Sci.* **114**, 5089–5094 (2017).
15. Huang, M.-J., Schofield, J. & Kapral, R. Chemotactic and hydrodynamic effects on collective dynamics of self-diffusiophoretic janus motors. *New J. Phys.* **19**, 125003 (2017).
16. Palacci, J. et al. Artificial rheotaxis. *Sci. Adv.* **1**, e1400214 (2015).
17. Baker, R. et al. Fight the flow: the role of shear in artificial rheotaxis for individual and collective motion. *Nanoscale* **11**, 10944–10951 (2019).
18. Pourrahimi, A. M. & Pummer, M. Multifunctional and self-propelled spherical janus nano/micromotors: recent advances. *Nanoscale* **10**, 16398–16415 (2018).
19. Ghosh, A. & Fischer, P. Controlled propulsion of artificial magnetic nanostructured propellers. *Nano Lett.* **9**, 2243–2245 (2009).
20. Wang, W., Chiang, T.-Y., Velegol, D. & Mallouk, T. E. Understanding the efficiency of autonomous nano- and microscale motors. *J. Am. Chem. Soc.* **135**, 10557–10565 (2013).
21. Brooks, A. M., Sabrina, S. & Bishop, K. J. Shape-directed dynamics of active colloids powered by induced-charge electrophoresis. *Proc. Natl Acad. Sci.* **115**, E1090–E1099 (2018).
22. Wang, X. et al. Surface-chemistry-mediated control of individual magnetic helical microswimmers in a swarm. *ACS nano* **12**, 6210–6217 (2018).
23. Baker, R. D. et al. Shape-programmed 3d printed swimming microtori for the transport of passive and active agents. *Nat. Commun.* **10**, 1–10 (2019).
24. Popescu, M. N., Dietrich, S. & Oshanin, G. Confinement effects on diffusiophoretic self-propellers. *J. Chem. Phys.* **130**, 194702 (2009).
25. Das, S. et al. Boundaries can steer active janus spheres. *Nat Commun* **6**, 8999 (2015).
26. Ibrahim, Y. & Liverpool, T. How walls affect the dynamics of self-phoretic microswimmers. *Eur. Phys. J. Special Topics* **225**, 1843 (2016).
27. Popescu, M. N., Uspal, W. E. & Dietrich, S. Self-diffusiophoresis of chemically active colloids. *Eur. Phys. J. Special Topics* **225**, 2189 (2016).
28. Shen, Z., Wurger, A. & Lintuvuori, J. S. Hydrodynamic interaction of a self-propelling particle with a wall. *Eur. Phys. J. E* **41**, 39 (2018).
29. Popescu, M. N., Uspal, W. E., Domínguez, A. & Dietrich, S. Effective interactions between chemically active colloids and interfaces. *Acc. Chem. Res.* **51**, 2991 (2018).
30. Or, Y. & Murray, R. M. Dynamics and stability of a class of low reynolds number swimmers near a wall. *Phys. Rev. E* **79**, 045302(R) (2009).
31. Or, Y., Zhang, S. & Murray, R. M. Dynamics and stability of low-reynolds-number swimming near a wall. *SIAM J. Appl. Dyn. Sys.* **10**, 1013 (2011).
32. Johnson, R. E. & Wu, T. Y. Hydromechanics of low-reynolds-number flow. part 5. motion of a slender torus. *J. Fluid Mech.* **95**, 263 (1979).
33. Thaokar, R. M. & Rochish, M. Brownian motion of a torus. *Colloids and Surfaces A: Physicochem. Eng. Aspects* **317**, 650 (2008).
34. Thaokar, R., Schiessel, H. & Kulic, I. Hydrodynamics of a rotating torus. *Eur. Phys. J. B* **60**, 325 (2007).
35. Moshkin, N. P. & Suwannaasri, P. Self-propelled motion of a torus rotating about its centerline in a viscous incompressible fluid. *Phys. Fluids* **22**, 113602 (2010).
36. Leshansky, A. M. & Kenneth, O. Surface tank treading: propulsion of purcell’s toroidal swimmer. *Phys. Fluids* **20**, 063104 (2006).
37. Schmieding, L. C., Lauga, E. & Montenegro-Johnson, T. D. Autophoretic flow on a torus. *Phys. Rev. Fluids* **2**, 034201 (2017).
38. Malevanets, A. & Kapral, R. Mesoscopic model for solvent dynamics. *J. Chem. Phys.* **110**, 8605–8613 (1999).
39. Kapral, R. Multiparticle collision dynamics: simulation of complex systems on mesoscales. *Adv. Chem. Phys.* **140**, 89–146 (2008).
40. Gompper, G., Ihle, T., Kroll, D. M. & Winkler, R. G. Multi-particle collision dynamics: a particle-based mesoscale simulation approach to the hydrodynamics of complex fluids. *Adv. Polym. Sci.* **221**, 1–87 (2009).
41. Wang, J., Huang, M.-J. & Kapral, R. Self-propelled torus colloids. *J. Chem. Phys.* **153**, 014902 (2020).
42. Anderson, J. L. Colloid transport by interfacial forces. *Annu. Rev. Fluid Mech.* **21**, 61–99 (1989).
43. Golestanian, R., Liverpool, T. B. & Ajdari, A. Propulsion of a molecular machine by asymmetric distribution of reaction products. *Phys. Rev. Lett.* **94**, 220801 (2005).
44. Gaspard, P. & Kapral, R. Thermodynamics and statistical mechanics of chemically powered synthetic nanomotors. *Advances in Physics: X* **4**, 1602480 (2019).
45. Colberg, P. H. & Kapral, R. Many-body dynamics of chemically propelled nanomotors. *J. Chem. Phys.* **147**, 064910 (2017).
46. Huang, M.-J., Schofield, J., Gaspard, P. & Kapral, R. From single particle motion to collective dynamics in janus motor systems. *J. Chem. Phys.* **150**, 124110 (2019).
47. Malevanets, A. & Kapral, R. Solute molecular dynamics in a mesoscale solvent. *J. Chem. Phys.* **112**, 7260–7269 (2000).
48. Rohlf, K., Fraser, S. & Kapral, R. Reactive multiparticle collision dynamics. *Comput. Phys. Commun.* **179**, 132–139 (2008).
49. Ihle, T. & Kroll, D. Stochastic rotation dynamics: a galilean-invariant mesoscopic model for fluid flow. *Phys. Rev. E* **63**, 020201 (2001).
50. Padding, J. T. & Louis, A. A. Hydrodynamic interactions and brownian forces in colloidal suspensions: coarse-graining over time and length scales. *Phys. Rev. E* **74**, 031402 (2006).

Acknowledgements

This work of R.K., J.W., and M.-J.H. was supported by a grant from the Natural Sciences and Engineering Research Council of Canada. Computations were performed on SciNet HPC Consortium computers. SciNet is funded by the Canada Foundation for Innovation through Compute Canada, the Government of Ontario, Ontario Research Excellence Fund and the University of Toronto. J.W. was supported by the Fundamental Research Funds for Heilongjiang Provincial Universities, No. 702/0000080914. The research of I.S.A. was supported by the U.S. Department of Energy, Office of Science, Basic Energy Sciences, under Award No. DE-SC0020964.

Author contributions

R.K. and I.S.A. designed the research, J.W. and M.J.H. performed computational study, J.W., M.J.H., R.D.B.S., R.K., I.S.A. discussed the results and wrote the paper.

Competing interests

The authors declare no competing interests.

Additional information

Supplementary information The online version contains supplementary material available at <https://doi.org/10.1038/s42005-022-00953-9>.

Correspondence and requests for materials should be addressed to Raymond Kapral or Igor S. Aranson.

Peer review information *Communications Physics* thanks the anonymous reviewers for their contribution to the peer review of this work.

Reprints and permission information is available at <http://www.nature.com/reprints>

Publisher’s note Springer Nature remains neutral with regard to jurisdictional claims in published maps and institutional affiliations.



Open Access This article is licensed under a Creative Commons Attribution 4.0 International License, which permits use, sharing, adaptation, distribution and reproduction in any medium or format, as long as you give appropriate credit to the original author(s) and the source, provide a link to the Creative Commons license, and indicate if changes were made. The images or other third party material in this article are included in the article’s Creative Commons license, unless indicated otherwise in a credit line to the material. If material is not included in the article’s Creative Commons license and your intended use is not permitted by statutory regulation or exceeds the permitted use, you will need to obtain permission directly from the copyright holder. To view a copy of this license, visit <http://creativecommons.org/licenses/by/4.0/>.

© The Author(s) 2022